DOI: 10.19884/j.1672-5220.202511010

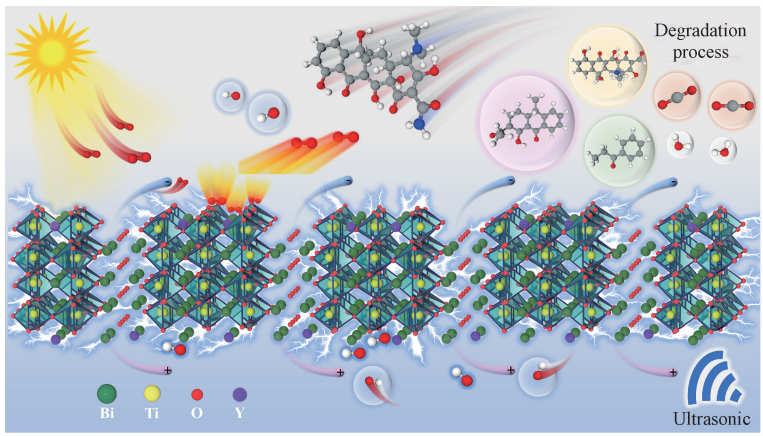
Polarization Enhancement in Y^{3+}-Doped Bismuth Titanate Nanosheets for Boosted Piezo-Photocatalytic Performance toward Efficient Water Purification

HANG Jiahe, HU Chunyan*, LIU Baojiang*
Key Laboratory of Sustainable Low-carbon Technologies for Textile Dyeing and Finishing, Ministry of Education, College of Chemistry and Chemical Engineering, Donghua University, Shanghai 201620, China

Abstract: The development of efficient piezo-photocatalytic systems is crucial for environmental remediation and the purification of wastewater. In this study, the yttrium ion (Y^{3+}) was introduced into the A-site of Aurivillius-phase bismuth titanate ($Bi_4Ti_3O_{12}$, BTO) via a structural modulation strategy to fabricate a novel piezo-photocatalyst (denoted as Y-BTO) for the synergistic degradation of tetracycline hydrochloride (TC). The results reveal that replacing Bi^{3+} with smaller-radius Y^{3+} not only induces lattice distortion but also enhances the intrinsic piezoelectric polarization within the material. Under simultaneous ultrasound and light irradiation, the optimally doped Y-BTO catalyst exhibits outstanding piezo-photocatalytic activity, achieving a TC removal rate of 88.8% within 60 min. The apparent pseudo-first-order rate constant for the piezo-photocatalytic degradation of TC is determined to be 29.40 × 10^{-3} min^{-1}, which is 3.6 and 2.3 times the values for individual piezocatalysis and photocatalysis, respectively. This remarkable enhancement is attributed to the piezo-photocatalytic synergy: the piezoelectric field generated by ultrasonic vibration effectively facilitates the separation and migration of photogenerated electron-hole pairs, thereby significantly improving the quantum efficiency. This study demonstrates that A-site ion substitution is an effective strategy for designing high-performance piezo-photocatalysts for environmental remediation.

Keywords: piezo-photocatalysis; wastewater treatment; polarization enhancement; Y^{3+}-doped bismuth titanate
CLC number: X703 **Document code:** A
Article ID: 1672-5220(2026)05-0001-13

Graphical abstract



0 Introduction

With the rapid development of the chemical, textile, and pharmaceutical industries, environmental pollution has become increasingly severe[1-3]. Industrial and domestic wastewater contains substantial amounts of organic pollutants, such as dyes[4] and antibiotics[5-6]. The long-term accumulation of these substances poses serious threats to human health and ecosystems[7]. Therefore, it is imperative to explore green and sustainable water treatment technologies for effective aquatic purification. Conventional wastewater treatment inadequately removes persistent organic pollutants,

Received date: 2025-11-19
* Correspondence should be addressed to HU Chunyan, email: chunyanhu@dhu.edu.cn; LIU Baojiang, email: bjliu@dhu.edu.cn
Citation: Hang J H, Hu C Y, Liu B J. Polarization enhancement in Y^{3+}-doped bismuth titanate nanosheets for boosted piezo-photocatalytic performance toward efficient water purification[J]. *Journal of Donghua University (English Edition)*, 2026, 43(5): 1-13.

thus necessitating advanced oxidation processes (AOPs). Among various AOPs, photocatalytic technology has been extensively studied due to its environmentally friendly and cost-effective characteristics. It utilizes clean solar energy to generate reactive oxygen species for degrading environmental pollutants[8-11]. However, the rapid recombination of photogenerated electron-hole pairs in semiconductor catalysts severely hinders their practical application efficiency[12].

Piezocatalysis has emerged as a promising approach, harnessing external mechanical energy (e. g., wind, water flow, tide, ultrasound, and stirring) to drive chemical reactions via the piezoelectric effect[13-16]. Nevertheless, the efficiency of sole piezocatalysis is often limited by the insufficient number of initial charge carriers. It is noteworthy that integrating photocatalysis and piezocatalysis into a piezo-photocatalytic system offers an effective pathway to overcome the limitations of conventional catalysis. On one hand, some piezoelectric materials with bandgaps of 2.5 – 3.5 eV inherently possess photocatalytic activity[17], and their built-in piezoelectric field can provide a strong driving force for the spatial separation of photogenerated carriers. On the other hand, structural modification of piezoelectric materials can further enhance this synergistic effect, significantly improving catalytic performance[18-20].

Ferroelectric materials with non-centrosymmetric structures are ideal candidates for piezo-photocatalysis. Bismuth titanate ($Bi_4Ti_3O_{12}$, BTO), a typical Aurivillius-phase perovskite, has attracted extensive attention due to its inherent ferroelectricity, chemical stability, and visible-light response[21-22]. However, the insufficient spontaneous polarization of pristine $Bi_4Ti_3O_{12}$ leads to suboptimal charge separation and consequently limits its catalytic efficacy. Researchers have adopted various strategies to address these limitations, such as ion doping[23-24], heterojunction construction[25], morphology control[26], and defect engineering[27-28]. Among them, A-site cation doping is regarded as a simple yet effective approach for modulating the electronic structure and optoelectronic properties of perovskite-structured materials. Precise A-site cation engineering enhances intrinsic dipole moment and polarization, thereby strengthening the piezoelectric field, which has been widely validated in perovskite systems. For instance, Yu et al.[29] prepared $BaTiO_3$ nanosheets via donor and acceptor ion doping, regulating their band structure and piezoelectric properties to achieve synergistic enhancement of piezo-photocatalytic performance. By leveraging band structure alignment, active species generation, and electrostatic adsorption matching, they realized selective degradation of anionic and cationic dyes, providing insights for the design of efficient environmental purification and hydrogen evolution catalysts. Nevertheless, systematic studies on the relationship between A-site ion doping and the piezo-photocatalytic activity of $Bi_4Ti_3O_{12}$ with similar perovskite-like structures remain relatively scarce. Currently, the structure-activity relationship between the yttrium ion (Y^{3+}) doping levels and the piezo-photocatalytic performance of $Bi_4Ti_3O_{12}$ remains unelucidated. This gap impedes a full grasp of structure-property correlations in bismuth-based layered perovskites and restricts their targeted design and practical application in pollution control.

Therefore, we propose an isovalent A-site substitution strategy by introducing Y^{3+} at the Bi-containing A-sites of $Bi_4Ti_3O_{12}$ to enhance piezoelectric polarization, thereby achieving piezo-photocatalytic performance. This study provides a high-performance Y^{3+}-doped $Bi_4Ti_3O_{12}$ piezo-photocatalyst (denoted as Y-BTO) for the efficient removal of aquatic pollutants. It also offers fundamental insights into the structure-activity relationships and reaction mechanisms in piezo-photocatalytic systems, providing valuable guidance for the rational design of advanced ferroelectric materials for environmental remediation.

1 Materials and Methods

1.1 Materials

Bismuth nitrate pentahydrate ($Bi(NO_3)_3 \cdot 5H_2O$), yttrium nitrate hexahydrate ($Y(NO_3)_3 \cdot 6H_2O$), tetrabutyl titanate ($Ti(OC_4H_9)_4$), and tetracycline hydrochloride (TC, $C_{22}H_{25}ClN_2O_8$) were purchased from Aladdin Chemical Co., Ltd., China. Sodium oleate ($C_{18}H_{33}NaO_2$) was purchased from Titan Scientific Co., Ltd., China. Absolute ethanol (C_2H_5OH), nitric acid (HNO_3), and sodium hydroxide (NaOH) were purchased from Sinopharm Chemical Reagent Co., Ltd., China. All chemicals were of analytical grade and used without further purification.

1.2 Synthesis of samples

Y-BTO nanosheets were synthesized via a hydrothermal method. As illustrated in Fig. 1, 1.69 mL $Ti(OC_4H_9)_4$ was dissolved in 20 mL dilute HNO_3 to form solution A. Subsequently, 12 g NaOH was dissolved in 20 mL deionized water to prepare solution B. $Y(NO_3)_3 \cdot 6H_2O$ (x mmol) and $Bi(NO_3)_3 \cdot 5H_2O$ ($4-x$ mmol, $x=0$, 0.4, 0.6, 0.8) were dissolved in 20 mL dilute HNO_3 solution (designated as solution C). Then, 30 mg sodium oleate was added to solution C and the mixture was stirred for 10 min to achieve homogeneous dispersion. Solutions A and B were slowly added dropwise to solution C under continuous stirring. The mixture was sonicated for 15 min and stirred at room temperature for 30 min before being transferred into a 100 mL Teflon-lined autoclave, and then heated at 180 ℃ for 20 h. After the reaction, the system was naturally cooled to room temperature. The resulting products were collected by vacuum filtration and washed three times with deionized water and C_2H_5OH. Finally, the products were dried at 60 ℃ under vacuum for 8 h to obtain the final samples,

labeled as BTO, 0.4Y-BTO, 0.6Y-BTO, and 0.8Y-BTO, respectively.

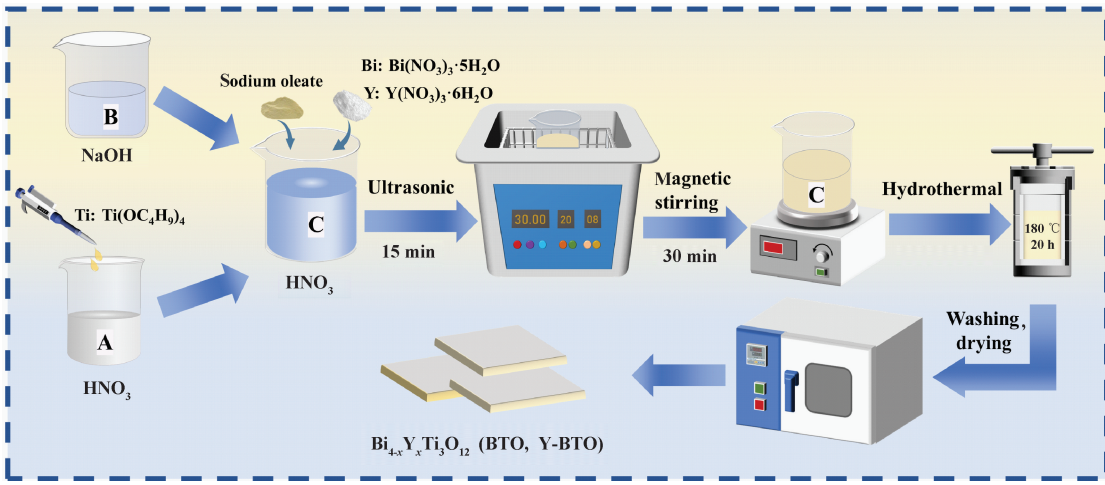


Fig. 1 Schematic illustration of synthesis procedure for BTO and Y-BTO samples

1.3 Characterization

The crystal structure and phase composition of the samples were characterized by an X-ray diffractometer (D8 Advance, Bruker, Germany). The surface elemental composition and chemical states were analyzed using an X-ray photoelectron spectrometer (K-Alpha, Thermo Fisher Scientific, USA). The micro-morphologies of the samples were examined by a scanning electron microscope (GeminiSEM 360, Zeiss, Germany). The ultra-microstructure and elemental distribution were investigated through a transmission electron microscope (JEM-F200, JEOL Ltd., Japan) equipped with an energy-dispersive X-ray spectrometer. Optical absorption properties were measured by an ultraviolet-visible (UV-vis) diffuse reflectance spectrophotometer (UV-3600 PLUS, Shimadzu, Japan) using barium sulfate as a reference. The absorbance of degradation solutions was monitored with a UV-vis spectrophotometer (UV-2365, UNICO, China). Active oxygen species generated during the catalytic degradation process were detected by an electron paramagnetic resonance (EPR) spectrometer (EMXplus-6/1, Bruker BioSpin, Germany). Electrochemical properties were evaluated using an electrochemical workstation (CHI760F, CH Instruments, China). The piezoelectric performance was characterized by an atomic force microscope (MFP-3D Origin+, Asylum Research, USA) under piezoresponse force microscopy (PFM) mode.

1.4 Experimental procedure

To investigate the piezo-photocatalytic performance of the catalysts, TC was selected as the target pollutant. An ultrasonic cleaner (110 W, 53 kHz) was employed to simulate external mechanical excitation, and a 300 W xenon lamp ($\lambda>400$ nm, 1 000 W/m^2) served as the external light source for evaluating the degradation efficiency. Specifically, 30 mg catalyst powder was first dispersed in 50.0 mL TC solution (30 mg/L) and subjected to dark adsorption for 30 min. Then, 3.5 mL suspension was withdrawn for the evaluation of adsorption performance. Subsequently, the mixture in the reactor was exposed simultaneously to ultrasonic irradiation and xenon lamp illumination for the piezo-photocatalytic reaction. Every 15 min, 3.5 mL suspension was collected, filtered through a 0.22 μm membrane, and analyzed using a UV-vis spectrophotometer by measuring the absorbance at the characteristic wavelength of TC (357 nm). The experimental procedures for piezocatalysis and photocatalysis were conducted under identical conditions. The degradation efficiency D of TC was calculated as

$$D=\frac{C_0-C}{C_0}=\frac{A_0-A}{A_0}, \quad (1)$$

where C_0 and C represent the initial concentration and the concentration of TC during the degradation process, respectively; A_0 and A denote the initial absorbance and the absorbance of TC during the degradation process, respectively.

2 Results and Discussion

2.1 Catalyst characterization

The morphologies and microstructures of BTO and 0.6Y-BTO samples were characterized using scanning electron microscopy (SEM) and transmission electron microscopy (TEM). As shown in Figs. 2(a) and 2(d), both samples exhibit a typical two-dimensional (2D) nanosheet structure, indicating that the ion doping does not alter the fundamental micro-morphology. The corresponding TEM images in Figs. 2(b) and 2(e) further confirm this nanosheet-like morphology. A reduction in the lateral dimensions of the nanosheets is observed after Y^{3+} doping, which may be attributed to the inhibited grain growth during the hydrothermal process due to the incorporation of Y^{3+}. High-resolution TEM

(HRTEM) analysis reveals changes at the lattice level. In Fig. 2(c), the lattice fringes with an interplanar spacing $d_{(200)}$ of 0.272 nm correspond to the (200) crystal plane of BTO. In contrast, for 0.6Y-BTO (Fig. 2(f)), the interplanar spacing of the (200) plane decreases to 0.254 nm. This lattice contraction provides direct evidence at the atomic scale for the successful substitution of smaller Y^{3+} into the Bi^{3+} lattice sites. Furthermore, energy-dispersive X-ray spectroscopy (EDS) elemental distribution mappings of 0.6Y-BTO (Fig. 2(g)) demonstrate a homogeneous distribution of Bi, Ti, O, and Y elements within the nanosheet, confirming the uniform doping of Y^{3+} into the BTO lattice.

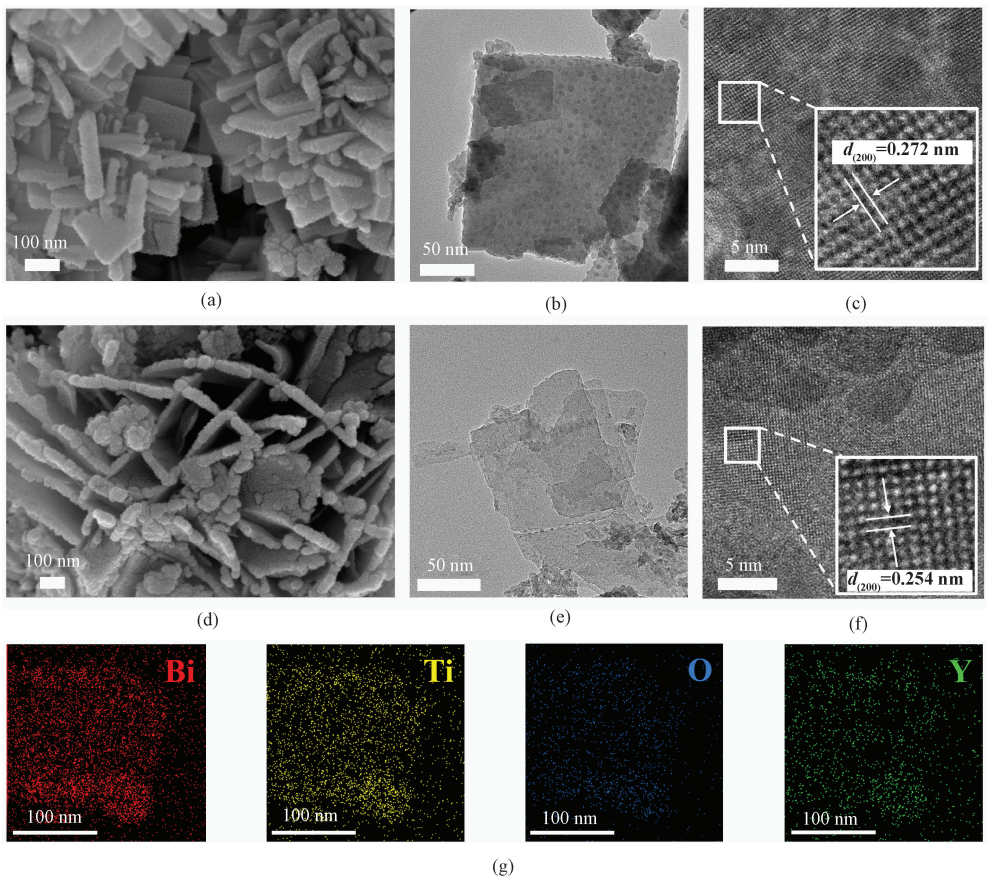


Fig. 2 Morphological and structural characterizations of BTO and 0.6Y-BTO: (a)–(c) SEM, TEM, and HRTEM images of BTO, respectively; (d)–(f) SEM, TEM, and HRTEM images of 0.6Y-BTO, respectively; (g) EDS elemental distribution maps of 0.6Y-BTO

Figure 3(a) shows XRD patterns of BTO and Y-BTO samples with different doping concentrations. All samples exhibit characteristic peaks of the Aurivillius-phase layered perovskite structure, showing good agreement with standard diffraction data (PDF#00-035-0795). The absence of impurity peaks confirms successful Y^{3+} doping at the A-site[30]. However, the decreased peak intensity and broadening after Y^{3+} doping suggest reduced crystallinity.

X-ray photoelectron spectroscopy (XPS) was performed to investigate the influence of Y^{3+} doping on the electronic structure and chemical states. The survey spectra (Fig. 3(b)) confirm that BTO contains Bi, Ti, and O, aside from adventitious C, while 0.6Y-BTO exhibits additional Y 3p and Y 3d peaks without any impurity-related signals. High-resolution spectra of Bi 4f, Ti 2p, O 1s, and Y 3p are shown in Figs. 3(c)–3(f), respectively. In Bi 4f spectra (Fig. 3(c)), BTO shows peaks at 158.90 eV (Bi $4f_{7/2}$) and 164.20 eV (Bi $4f_{5/2}$), corresponding to Bi^{3+}[24]. For 0.6Y-BTO, these peaks shift slightly to higher binding energies (159.12 and 164.25 eV), indicating a reduced local electron density around Bi atoms and electronic rearrangement in the Bi—O bonding environment due to Y^{3+} incorporation. Additionally, characteristic Y $3d_{5/2}$ and Y $3d_{3/2}$ peaks appear at 157.22 and 158.75 eV, consistent with Y^{3+}, further confirming substitution of Bi^{3+} by Y^{3+}. The Ti 2p spectrum (Fig. 3(d)) displays peaks at 457.85 eV (Ti $2p_{3/2}$) and 463.54 eV (Ti $2p_{1/2}$) for BTO, with a spin-orbit splitting of about 5.7 eV, characteristic of Ti^{4+}[31]. For 0.6Y-BTO, both peaks shift slightly toward higher binding energies, suggesting that Y^{3+} doping induces local lattice contraction and electrostatic potential changes, thereby affecting the Ti—O coordination environment. The O 1s spectra (Fig. 3(e)) are deconvoluted into lattice oxygen (O_L)

and surface hydroxyl (O—H) components. For 0.6Y-BTO, the O_L peak shifts to 529.67 eV, and the intensity of the O—H peak increases, reflecting enhanced surface active sites and polarity after Y^{3+} doping[32]. The Y 3p spectrum (Fig. 3(f)) shows no signal in BTO, while 0.6Y-BTO exhibits sharp Y $3p_{3/2}$ and Y $3p_{1/2}$ peaks at 300.35 and 312.20 eV, respectively, consistent with Y^{3+}[33] and confirming homogeneous distribution and stable valence of Y^{3+} in the lattice.

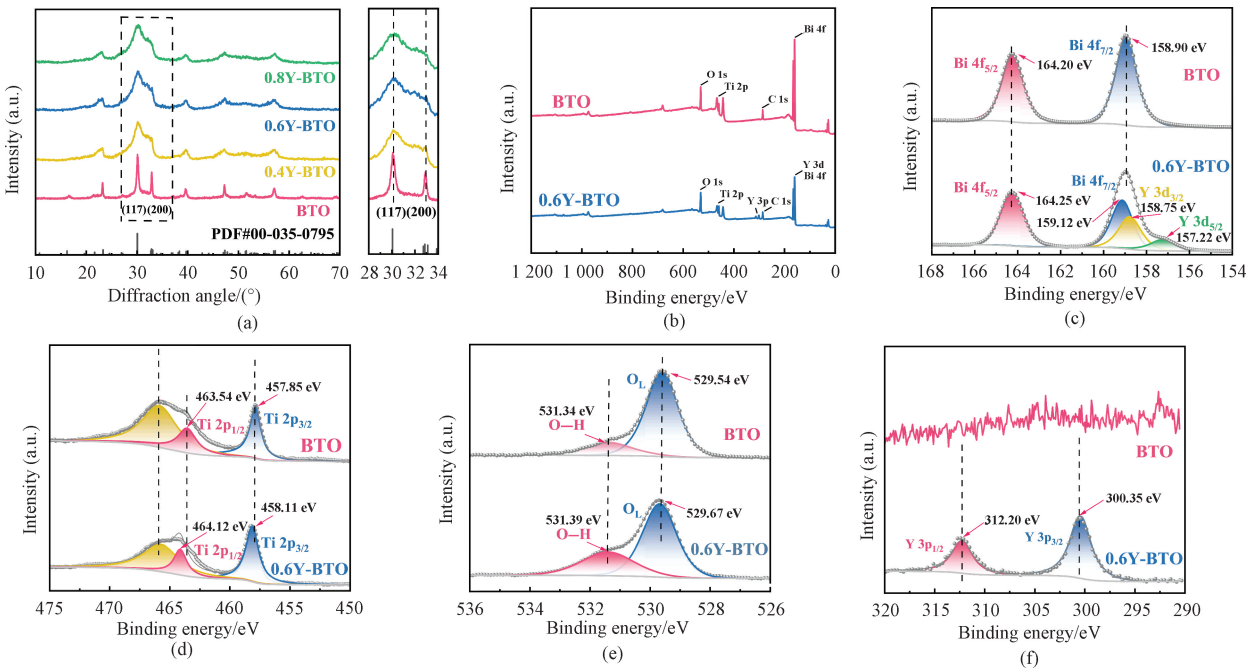


Fig. 3 Phase structure and surface chemical state analyses: (a) XRD patterns; (b) XPS survey spectra; (c) XPS high-resolution Bi 4f spectra; (d) XPS high-resolution Ti 2p spectra; (e) XPS high-resolution O 1s spectra; (f) XPS high-resolution Y 3p spectra

To elucidate the light absorption characteristics of the catalysts, UV-vis diffuse reflectance spectroscopy was conducted. As shown in Fig. 4(a), compared to BTO, 0.6Y-BTO exhibits a distinct blue-shift in the absorption edge. The bandgap energy E_g values of BTO and 0.6Y-BTO are determined to be 3.15 and 3.07 eV, respectively, based on Tauc plot analysis (Fig. 4(b)). Here, α, h, and ν represent the absorption coefficient, Planck's constant, and photon frequency, respectively. The E_g values were obtained by extrapolating the linear portion of the $(\alpha h\nu)^{1/2}$ versus $h\nu$ plots. This bandgap narrowing is primarily attributed to the lattice distortion and electronic structure reorganization induced by Y^{3+} doping, which enhances the visible-light harvesting capability.

Mott-Schottky measurements (Fig. 4(c)) reveal typical n-type semiconductor characteristics for both BTO and 0.6Y-BTO. The flat-band potentials versus Ag/AgCl were determined to be −1.18 V for BTO and −1.25 V for 0.6Y-BTO. These values are converted to the normal hydrogen electrode (NHE) scale using the equation $E_{NHE} = E_{Ag/AgCl} + 0.197$ V, where E_{NHE} is the potential on the NHE scale, and $E_{Ag/AgCl}$ denotes the potential measured against the Ag/AgCl reference electrode, yielding about −0.98 V for BTO and −1.05 V for 0.6Y-BTO. For n-type semiconductors, the conduction-band minimum potential E_{CB} is typically 0.1 – 0.2 V more negative than the flat-band potential[34]. Herein, an offset of 0.1 V is adopted. Based on this empirical relationship, the E_{CB} values are estimated to be −1.08 V for BTO and −1.15 V for 0.6Y-BTO versus NHE. The valence-band maximum energy E_{VB} values are then calculated to be 2.07 eV for BTO and 1.92 eV for 0.6Y-BTO. The energy band structures are illustrated in Fig. 4(d). Both BTO and 0.6Y-BTO exhibit conduction-band potentials more negative than the $O_2/O_2^{\cdot-}$ redox potential (−0.33 V vs. NHE) and valence-band potentials more positive than the $OH^-/\cdot OH$ potential (1.90 V vs. NHE), indicating sufficient thermodynamic driving force for generating superoxide radicals ($O_2^{\cdot-}$) and hydroxyl radicals ($\cdot OH$). Notably, the more negative conduction band of 0.6Y-BTO provides stronger reducing power for O_2 reduction to $O_2^{\cdot-}$, consistent with the enhanced photocatalytic performance and radical trapping experiments. Electrochemical impedance spectroscopy (Fig. 4(e)) shows the Nyquist plots, where Z' and Z'' denote the real and imaginary components of the alternating-current (AC) impedance, and the vertical axis corresponds to $-Z''$. Compared with BTO, 0.6Y-BTO exhibits a smaller semicircular arc radius, which suggests a lower charge-transfer resistance. The transient photocurrent responses (Fig. 4(f)) show that 0.6Y-BTO maintains a stable and enhanced photocurrent density over multiple on-off cycles, suggesting improved charge separation efficiency and suppressed carrier recombination. These

electrochemical results collectively confirm that Y^{3+} doping effectively enhances the photogenerated charge separation and transfer in the BTO system. In summary, Y^{3+} doping not only optimizes the band structure and light absorption characteristics but also significantly improves the charge separation and transport efficiency in BTO.

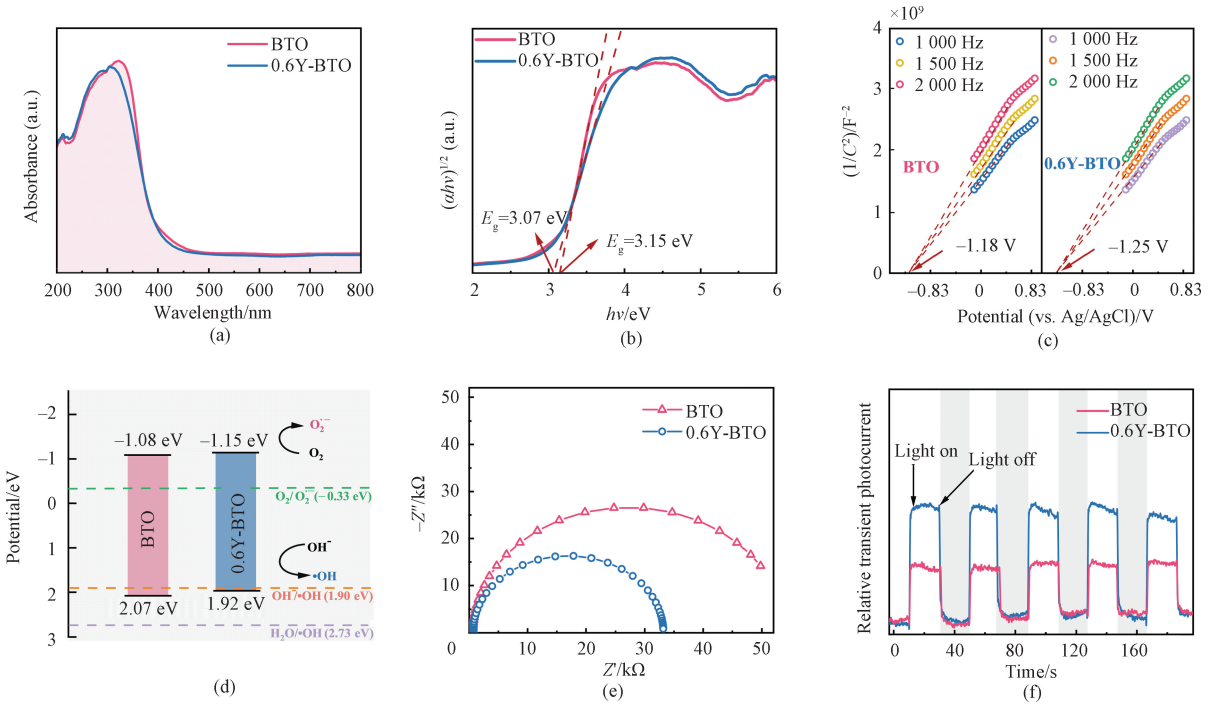
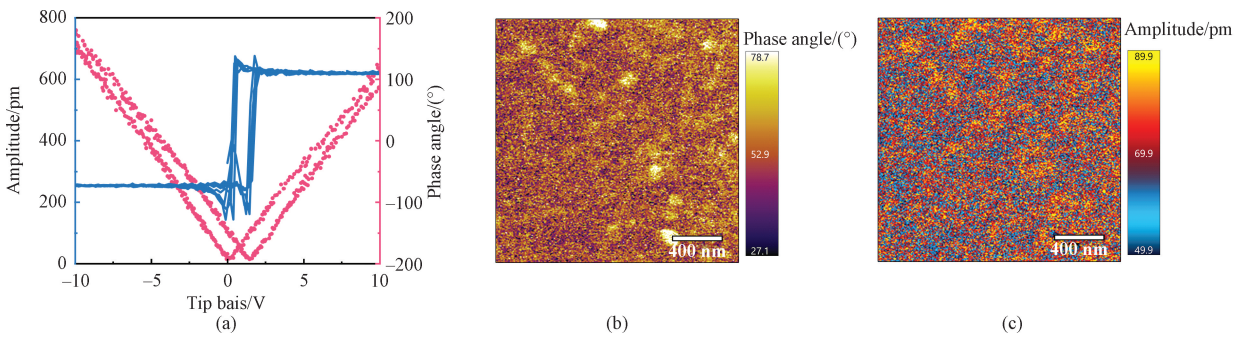


Fig. 4 Photoelectrochemical properties of BTO and 0.6Y-BTO: (a) UV-vis diffuse reflectance spectra; (b) Tauc plots; (c) Mott-Schottky plots; (d) band structure schematic; (e) electrochemical impedance analysis; (f) transient photocurrent responses

Piezoelectric performance is one of the key factors determining the efficiency of piezoelectric-assisted photocatalysis[35-36]. To evaluate the effect of Y^{3+} doping on the piezoelectric properties of BTO, this study employed PFM to characterize the local piezoelectric responses of BTO and 0.6Y-BTO under identical bias conditions (±10 V). As shown in Figs. 5(a) and 5(d), both BTO and 0.6Y-BTO exhibit typical butterfly-shaped amplitude curves and hysteresis loops, confirming their intrinsic piezoelectric characteristics. The maximum amplitudes and corresponding voltages were measured to be 760.0 pm at −9.93 V for BTO and 2 063.0 pm at −9.76 V for 0.6Y-BTO, from which the piezoelectric coefficients d_{33} were calculated to be 76.5 and 211.4 pm/V, respectively. Evidently, Y^{3+} doping enhances the piezoelectric response of the material by nearly 2.8 times, demonstrating a significant performance improvement. Figures 5(b) and 5(e) show the phase images of BTO and 0.6Y-BTO, respectively. The consistent phase contrast between BTO and 0.6Y-BTO indicates that Y^{3+} doping does not alter the polarization orientation of BTO, implying stable ferroelectric domain structures. However, as shown in Figs. 5(c) and 5(f), a notable difference is observed in the amplitude images. The maximum amplitude of BTO is 89.9 pm with a spatial contrast of 40.0 pm, while that of 0.6Y-BTO reaches 178.0 pm with an enhanced spatial contrast of 93.5 pm. This remarkable improvement suggests that the introduction of Y^{3+} strengthens lattice distortion and increases the local strain gradient, thereby amplifying the piezoelectric polarization response. The enhanced piezoelectric polarization field provides a strong driving force for the separation of photogenerated charge carriers.



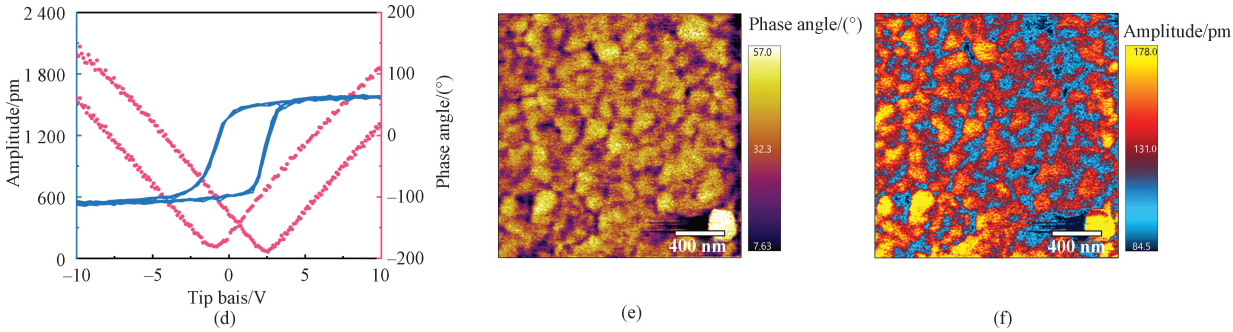
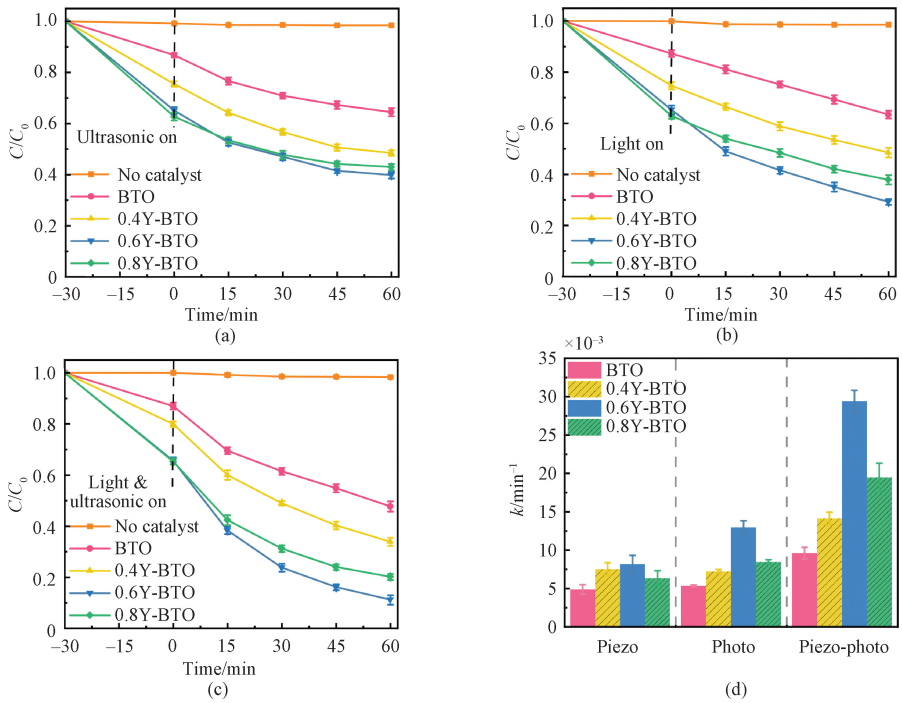


Fig. 5 PFM analyses: (a) butterfly-shaped amplitude curve and hysteresis loop of BTO; (b) phase image of BTO; (c) amplitude image of BTO; (d) butterfly-shaped amplitude curve and hysteresis loop of 0.6Y-BTO; (e) phase image of 0.6Y-BTO; (f) amplitude image of 0.6Y-BTO

2.2 Evaluation of piezocatalytic, photocatalytic, and piezo-photocatalytic performance

Figure 6(a) shows the piezocatalytic degradation experiments under ultrasonic excitation alone. The degradation of TC is negligible without catalysts, confirming that ultrasound itself cannot effectively degrade TC. The time window of −30 to 0 min denotes the dark-adsorption phase without external stimulus. Ultrasonic excitation is activated at 0 min to trigger the piezocatalytic reaction. During this prior 30 min dark-adsorption phase, both BTO and Y-BTO exhibit certain adsorption capacity toward TC, which gradually increases and stabilizes with higher Y^{3+} doping levels. This enhancement is attributed to the lattice structure modulation induced by Y^{3+} doping, which increases the specific surface area and pore volume of the nanosheets while reducing their lateral dimensions. Throughout the degradation period of 60 min, both BTO and Y-BTO demonstrate measurable piezocatalytic activity. As a typical ferroelectric material, BTO exhibits spontaneous polarization at room temperature, enabling piezoelectric responses[37-38]. With increasing Y^{3+} doping content, enhanced lattice distortion strengthens the piezoelectric polarization, leading to significantly improved piezocatalytic degradation performance. Among all samples, 0.6Y-BTO achieves the optimal degradation efficiency, reaching 60.2% TC removal within 60 min, with an apparent pseudo-first-order rate constant k of 8.20×10^{-3} min^{-1}, approximately 1.7 times that of BTO (4.80×10^{-3} min^{-1}). For the photocatalytic system in Fig. 6(b), light irradiation is turned on at 0 min following the identical 30 min dark-adsorption phase. While for the piezo-photocatalytic test in Fig. 6(c), both light and ultrasonic excitation are introduced at 0 min after the same dark-adsorption phase. BTO exhibits limited catalytic degradation capability toward TC under visible-light irradiation due to the inherent wide bandgap, which restricts visible-light absorption. Y^{3+} doping effectively modulates the band structure of BTO, resulting in a narrowed bandgap and a negatively shifted conduction-band position. These changes enhance both visible-light absorption and the redox activity of photogenerated charge carriers, thereby significantly improving the photocatalytic performance. Among various doping contents, 0.6Y-BTO again demonstrates the best performance, achieving 70.8% TC degradation within 60 min with an apparent pseudo-first-order rate constant of 13.00×10^{-3} min^{-1}, about 2.5 times that of BTO (5.30×10^{-3} min^{-1}). Further increasing the Y^{3+} doping content leads to a slight decline in activity, likely due to the introduction of defect centers that promote charge carrier recombination. In the piezo-photocatalytic system (Fig. 6(c)), the degradation performance of Y-BTO is further enhanced, indicating a clear synergistic effect between the piezoelectric field and photogenerated carriers. The transient piezoelectric potential generated by ultrasonic excitation promotes the separation of electron-hole pairs and suppresses their recombination, thereby improving the overall catalytic efficiency. Remarkably, 0.6Y-BTO achieves 88.8% TC degradation within 60 min, with an apparent pseudo-first-order rate constant of 29.40×10^{-3} min^{-1}, approximately 3.6 and 2.3 times those of individual piezocatalysis and photocatalysis, respectively. This result highlights the significant enhancement arising from the synergistic effect. A comparison of the apparent pseudo-first-order rate constants is summarized in Fig. 6(d).



Piezo—piezocatalysis; Photo—photocatalysis; Piezo-photo—piezo-photocatalysis.

Fig. 6 Degradation performance: (a) piezocatalysis; (b) photocatalysis; (c) piezo-photocatalysis; (d) apparent pseudo-first-order rate constants under various degradation conditions

To further investigate the piezo-photocatalytic performance of Y-BTO under different environmental conditions, this study selected 0.6Y-BTO as a representative catalyst and TC as the target pollutant to examine the influence of key factors—including the catalyst dosage, electrolyte type, solution pH, and cycling stability—on the reaction activity.

As shown in Fig. 7(a), the degradation efficiency of TC gradually increases and eventually reaches saturation with increasing catalyst dosage. At 30 mg, the degradation efficiency achieves 88.8% with an apparent pseudo-first-order rate constant of 29.40×10^{-3} min^{-1}. However, further increasing the catalyst dosage to 40 mg results in only a marginal improvement in the degradation efficiency. This saturation behavior can be attributed to two main factors. First, when the catalyst dosage exceeds the critical light-scattering threshold, increased turbidity of the suspension reduces light penetration depth, thereby limiting the generation and migration of photogenerated charge carriers[39]. Second, excess catalyst loading induces agglomeration, blocks active sites via competitive adsorption, and limits performance. Waterborne inorganic ions also impact catalytic reactions.

As shown in Fig. 7(b), the presence of these electrolytes results in varying degrees of reduction in TC degradation efficiency. This phenomenon is primarily attributed to the competitive adsorption between anions (Cl^-, CO_3^{2-}, and SO_4^{2-}) and TC molecules or active sites on the catalyst surface, which reduces the available reactive area and consequently inhibits the catalytic degradation process. Furthermore, Cl^- and CO_3^{2-} readily react with photogenerated holes (h^+), diminishing their oxidative capacity[40], while SO_4^{2-} may suppress the electron transfer process, thereby reducing the generation rate of $O_2^{\cdot -}$ and weakening the reaction efficiency[41]. The solution pH serves as another critical factor governing piezo-photocatalytic performance. As illustrated in Fig. 7(c), the enhancement of alkalinity significantly improved the degradation efficiency. On one hand, the alkaline environment favors the generation of $O_2^{\cdot -}$, which serves as the primary active species for TC degradation. On the other hand, the electron cloud density of TC molecules increases under alkaline conditions, making them more susceptible to reaction with oxidative radicals and thereby accelerating the degradation process[42]. These results demonstrate that moderately alkaline conditions are conducive to activating the piezo-photocatalytic potential of the Y-BTO system. The cycling stability of a catalyst is a crucial indicator for evaluating its reusability. As shown in Fig. 7(d), during five consecutive cycling tests, the catalytic activity of 0.6Y-BTO exhibits only a slight decline, with the TC degradation efficiency decreasing from 89.3% in the first cycle to 77.2% in the fifth cycle. The observed activity attenuation can be primarily attributed to partial loss of the powdered catalyst during recovery, as well as the possible deactivation of some active sites due to repeated ultrasonic treatment and particle agglomeration during the reaction process. In summary, 0.6Y-BTO demonstrates outstanding piezo-photocatalytic

performance across diverse environmental conditions, highlighting its promising application potential and environmental adaptability for aquatic pollutant remediation.

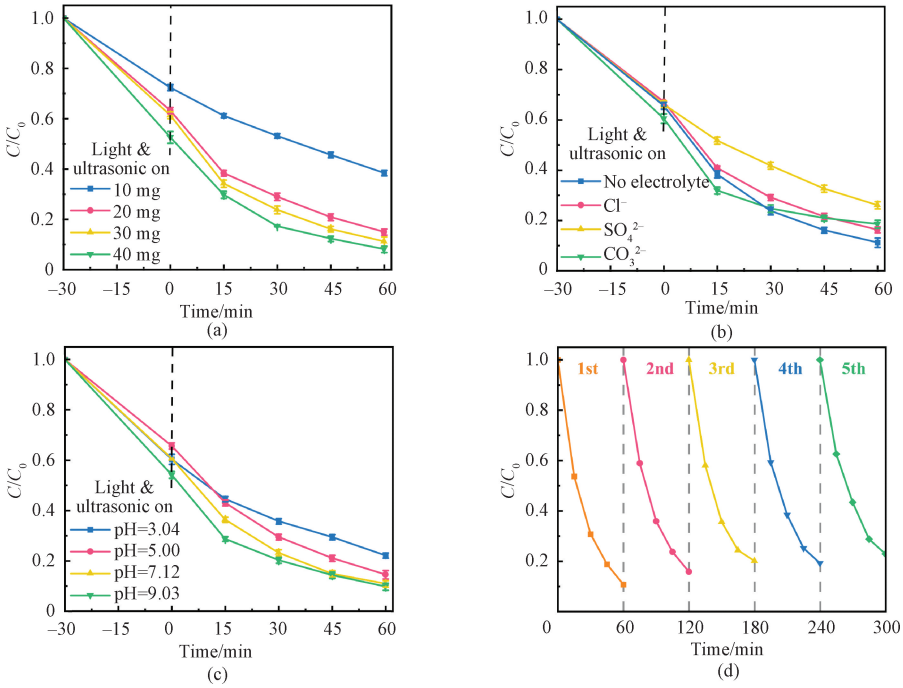


Fig. 7 Evaluation of degradation performance and stability: (a) catalyst dosage; (b) electrolyte type; (c) solution pH; (d) cycling stability

2.3 Active species analysis

In the radical trapping experiments, TC remained the target pollutant. Tert-butanol (TBA), *p*-benzoquinone (*p*-BQ), and sodium oxalate (Na-OA) were used as scavengers for ·OH, $O_2^{\cdot-}$, and h^+, respectively, each at a concentration of 0.05 mol/L. The catalyst dosage was fixed at 30 mg for all trapping experiments. As shown in Figs. 8(a) and 8(b), the addition of scavengers inhibits the degradation efficiency of TC to varying degrees in both photocatalytic and piezo-photocatalytic systems, with consistent trends observed across conditions. This indicates that reactive radicals play a critical role in the degradation process, and the introduction of a piezoelectric field does not alter the dominant active species in the reaction system. The apparent pseudo-first-order rate constants derived from the radical trapping experiments are summarized in Fig. 8(c). Under the synergistic effect of light and ultrasonic excitation, the apparent pseudo-first-order rate constants are significantly higher than those under photocatalytic conditions alone. This demonstrates that the piezoelectric field effectively promotes the separation and migration of charge carriers, thereby enhancing the generation rate of active species. Specifically, in the piezo-photocatalytic system, the addition of *p*-BQ, TBA, and Na-OA reduces the apparent pseudo-first-order rate constants to 3.56×10^{-3}, 25.18×10^{-3}, and 17.87×10^{-3} min^{-1}, respectively. In contrast, the corresponding values under photocatalytic conditions are 2.88×10^{-3}, 10.40×10^{-3}, and 8.37×10^{-3} min^{-1}. The most significant suppression is observed with *p*-BQ addition, followed by Na-OA, while TBA shows the least inhibitory effect. These results indicate that $O_2^{\cdot-}$ and h^+ serve as the primary active species in the piezo-photocatalytic degradation process, while ·OH plays a secondary role. To further verify the generation of reactive oxygen species, EPR tests with 5, 5-dimethyl-1-pyrroline *N*-oxide (DMPO) spin trapping were performed on 0.6Y-BTO. The results are shown in Figs. 8(d) and 8(e). Under dark conditions, no significant signals are detected. When light or ultrasonic excitation is applied individually, characteristic four-line DMPO-$O_2^{\cdot-}$ adduct signals are observed, indicating the generation of small amounts of $O_2^{\cdot-}$ under these single excitation conditions. Notably, under combined light and ultrasonic excitation, the $O_2^{\cdot-}$ signal intensity increases substantially, reaching approximately 1.5 times that under light irradiation alone. This demonstrates the significant promoting effect of the piezoelectric field on the separation of photogenerated electron-hole pairs and $O_2^{\cdot-}$ generation. Similarly, in the DMPO-·OH spectra, weak ·OH signals are detected under individual light or ultrasound conditions, while the signal intensity is enhanced markedly under simultaneous light and ultrasonic excitation. This further confirms the presence of ·OH and its synergistic oxidative role in the reaction system.

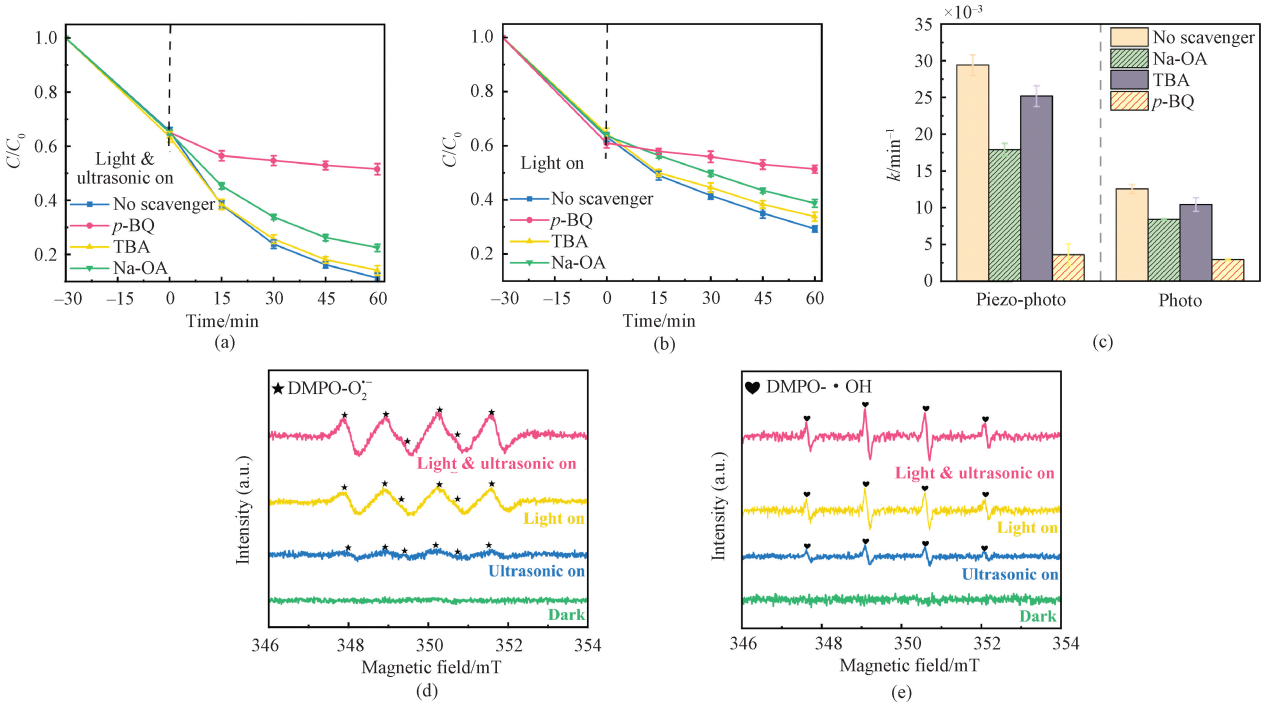


Fig. 8 Analysis of active species: (a) free radical trapping experiments in piezo-photocatalytic system; (b) free radical trapping experiments in photocatalytic system; (c) apparent pseudo-first-order rate constants from radical trapping experiments; (d) DMPO-$O_2^{\cdot-}$ EPR spectra; (e) DMPO-·OH EPR spectra

2.4 Analysis of catalytic mechanism

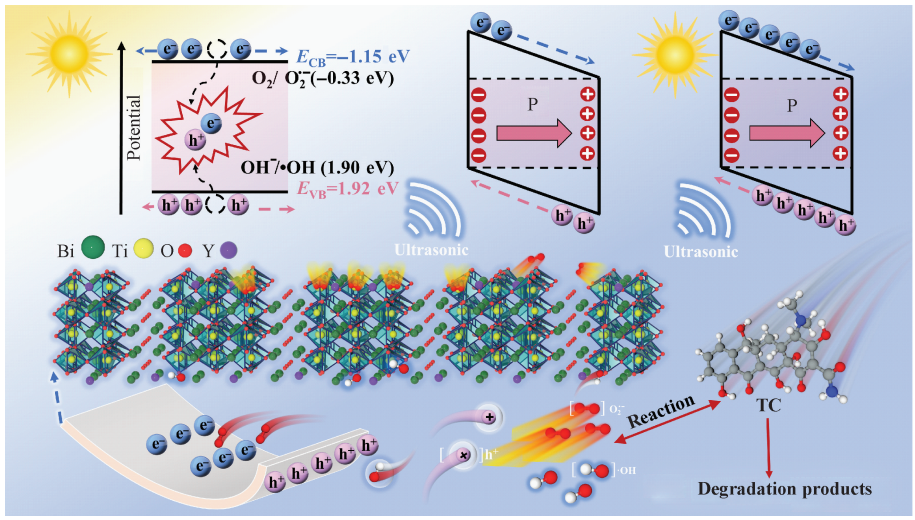
A schematic diagram of the proposed piezo-photocatalytic mechanism is presented in Fig. 9. Specifically, under visible light irradiation (λ>400 nm), 0.6Y-BTO absorbs photons and generates electron-hole pairs. In the absence of external stimulation, these carriers tend to recombine rapidly within the bulk phase, limiting the photocatalytic activity. Under sole ultrasonic excitation, the stress-induced deformation triggers a piezoelectric effect that can drive charge separation. However, the intrinsically low concentration of charge carriers excited by ultrasound alone results in weak piezocatalytic performance. Under simultaneous light and ultrasonic excitation (denoted as US/$h\nu$ in Eq. (2)), the incident photons generate abundant electron-hole pairs within 0.6Y-BTO. Concurrently, the strong piezoelectric field induced by the ultrasound not only provides a directional driving force for their spatial separation but also, due to its dynamic and transient nature, continuously directs electrons and holes toward oppositely polarized surfaces throughout the ultrasonic cycle. This synergistic effect effectively minimizes bulk charge recombination and enhances the availability of carriers for surface redox reactions. The photogenerated electrons migrate to the negatively polarized surface, where they reduce adsorbed O_2 molecules to form $O_2^{\cdot-}$, while the photogenerated holes migrate to the positively polarized surface and oxidize surface OH^- groups to produce ·OH. The resulting $O_2^{\cdot-}$, ·OH, and h^+ then collectively participate in redox reactions with organic pollutants, achieving efficient degradation. The detailed reaction process can be described as follows.

$$\text{Y-BTO} + (\text{US}/h\nu) \longrightarrow e^- + h^+, \quad (2)$$

$$O_2 + e^- \longrightarrow O_2^{\cdot-}, \quad (3)$$

$$OH^- + h^+ \longrightarrow \cdot OH, \quad (4)$$

$$\cdot OH,\ O_2^{\cdot-},\ h^+ + TC \longrightarrow \text{Degradation products}. \quad (5)$$



P—piezoelectric polarization.

Fig. 9 Proposed mechanism of piezo-photocatalytic degradation of TC over 0.6Y-BTO

3 Conclusions

Herein, Y-BTO nanosheets were synthesized hydrothermally, and the effect of different Y^{3+} doping contents on their piezo-photocatalytic degradation of TC was studied. Among all samples, 0.6Y-BTO exhibited outstanding piezo-photocatalytic activity, achieving a TC degradation efficiency of 88.8% within 60 min. The enhanced catalytic performance is attributed to the synergistic effects of Y^{3+} doping, which simultaneously enhances piezoelectric polarization, optimizes the band structure, and promotes the coupling between piezoelectric and photocatalytic processes. Through free radical trapping experiments and EPR analysis, $O_2^{\cdot -}$ and h^+ were identified as the dominant active species in the degradation process. This study elucidates the pivotal role of isovalent A-site doping in enhancing the piezoelectric effect, optimizing the electronic band structure, and facilitating efficient charge carrier separation. The findings offer valuable insights into the rational design of high-performance ferroelectric-based piezo-photocatalysts for environmental remediation and energy conversion applications.

References

[1] Georgin J, Franco D S P, Meili L, et al. Environmental remediation of the norfloxacin in water by adsorption: advances, current status and prospects[J]. *Advances in Colloid and Interface Science*, 2024, 324: 103096.

[2] Mechnou I, Meskini S, Elqars E, et al. Classical and advanced isotherms to model the adsorption of drugs, dyes and metals on activated carbonaceous materials: a review [J]. *Environmental Chemistry Letters*, 2024, 22(5): 2375-2404.

[3] Wang M R, Bodirsky B L, Rijneveld R, et al. A triple increase in global river basins with water scarcity due to future pollution [J]. *Nature Communications*, 2024, 15(1): 880.

[4] Zhai H, Liu Z K, Xu L L, et al. Waste textile reutilization via a scalable dyeing technology: a strategy to enhance dyestuffs degradation efficiency[J]. *Advanced Fiber Materials*, 2022, 4(6): 1595-1608.

[5] Ahmed M B, Zhou J L, Ngo H H, et al. Adsorptive removal of antibiotics from water and wastewater: progress and challenges[J]. *Science of the Total Environment*, 2015, 532: 112-126.

[6] Zhu Z X, Zhang X. Development of electrochemical sensor for cefadroxil antibiotic based on conductive carbon black decorated with tetrabutylammonium tetrafluoroborate [J]. *Journal of Donghua University (English Edition)*, 2025, 42(4): 348-357.

[7] Lin L, Yang H R, Xu X C. Effects of water pollution on human health and disease heterogeneity: a review [J]. *Frontiers in Environmental Science*, 2022, 10: 880246.

[8] Liang Y, Huang G H, Xin X Y, et al. Black titanium dioxide nanomaterials for photocatalytic removal of pollutants: a review[J]. *Journal of Materials Science & Technology*, 2022, 112: 239-262.

[9] Deng A X, Sun Y, Gao Z Q, et al. Internal electric field in carbon nitride-based heterojunctions for photocatalysis [J]. *Nano Energy*, 2023, 108: 108228.

[10] Nguyen T D, Nguyen V H, Nanda S, et al. $BiVO_4$ photocatalysis design and applications to oxygen production and degradation of organic

compounds: a review [J]. *Environmental Chemistry Letters*, 2020, 18(6): 1779-1801.
[11] Mirzaei A, Chen Z, Haghighat F, et al. Removal of pharmaceuticals and endocrine disrupting compounds from water by zinc oxide-based photocatalytic degradation: a review[J]. *Sustainable Cities and Society*, 2016, 27: 407-418.
[12] Zhang L Y, Zhang J J, Yu H G, et al. Emerging S-scheme photocatalyst[J]. *Advanced Materials*, 2022, 34(11): 2107668.
[13] Zhu Y Q, Chen H H, Wang L, et al. Piezoelectric materials for pollutants degradation: state-of-the-art accomplishments and prospects [J]. *Chinese Chemical Letters*, 2024, 35(4): 108884.
[14] Wang K, Han C, Li J Q, et al. The mechanism of piezocatalysis: energy band theory or screening charge effect? [J]. *Angewandte Chemie International Edition*, 2022, 61(6): e202110429.
[15] Wang M Y, Wang B, Huang F, et al. Enabling piezopotential in piezoelectric semiconductors for enhanced catalytic activities [J]. *Angewandte Chemie International Edition*, 2019, 131(23): 7606-7616.
[16] Zhu F S, Hu C Y, Liu B J. Piezo-photocatalytic technology based on bismuth ferrite ($Bi_2Fe_4O_9$) for degradation of reactive dye KN-R [J]. *Journal of Donghua University (English Edition)*, 2025, 42(1): 1-11.
[17] Zheng H J, Wang Y L, Liu J S, et al. Recent advancements in the use of novel piezoelectric materials for piezocatalytic and piezo-photocatalytic applications[J]. *Applied Catalysis B: Environmental*, 2024, 341: 123335.
[18] Gong S X, Zhang W X, Liang Z R, et al. Construction of a $BaTiO_3$/tubular g-C_3N_4 dual piezoelectric photocatalyst with enhanced carrier separation for efficient degradation of tetracycline [J]. *Chemical Engineering Journal*, 2023, 461: 141947.
[19] Liu Y, Zheng J, Zhu Z J, et al. Enhanced visible light responsive piezoelectric photocatalysis based on Bi_2S_3 coated $BaTiO_3$ nanorods heterostructures[J]. *Journal of Colloid and Interface Science*, 2025, 678: 657-670.
[20] Ning X E, Hao A Z, Chen R Q, et al. Constructing of GQDs/ZnO S-scheme heterojunction as efficient piezocatalyst for environmental remediation and understanding the charge transfer mechanism[J]. *Carbon*, 2024, 218: 118772.
[21] Wang C Y, Chen F, Hu C, et al. Efficient piezocatalytic H_2O_2 production of atomic-level thickness $Bi_4Ti_3O_{12}$ nanosheets with surface oxygen vacancy [J]. *Chemical Engineering Journal*, 2022, 431: 133930.
[22] Xie S X, Xu Q, Chen Q, et al. Realizing super-high piezoelectricity and excellent fatigue resistance in domain-engineered bismuth titanate ferroelectrics[J]. *Advanced Functional Materials*, 2024, 34(18): 2312645.
[23] Jing L X, Zhuang F, Feng W, et al. Doping-engineered piezoelectric ultrathin nanosheets for synergistically piezo-chemocatalytic antitumor and antibacterial therapies against cutaneous melanoma[J]. *Small*, 2024, 20(40): 2401171.
[24] Sun S H, Wang X, Chen Z W, et al. Piezoelectric enhanced photocatalytic degradation of levofloxacin by La doped $Bi_4Ti_3O_{12}$ nanosheets [J]. *Journal of Water Process Engineering*, 2024, 65: 105787.
[25] Fan H, Xu M J, Ai L L, et al. Photocatalyst for antibiotics degradation by in situ growth of direct Z-type Bi_2S_3/$Bi_4Ti_3O_{12}$ heterojunction [J]. *Inorganic Chemistry*, 2024, 63(46): 22088-22100.
[26] Zhong S, Liu L H, Liu G G, et al. Piezoelectric polarization promoted separation of photogenerated carriers in $Bi_{3.25}La_{0.75}Ti_3O_{12}$ with different micro-morphologies for efficient elimination of 2, 4-dichlorophenol and tetracycline[J]. *Journal of Cleaner Production*, 2022, 373: 133644.
[27] Tang Q, Wu J, Chen X Z, et al. Tuning oxygen vacancies in $Bi_4Ti_3O_{12}$ nanosheets to boost piezo-photocatalytic activity[J]. *Nano Energy*, 2023, 108: 108202.
[28] Zhu Q H, Wang Y, Wang J J, et al. Synergistic polarization and oxygen vacancies engineering for enhancing photocatalytic NO removal over $Bi_4Ti_3O_{12}$ nanowires [J]. *Applied Catalysis B: Environment and Energy*, 2024, 346: 123734.
[29] Yu C Y, He J J, Tan M X, et al. Selective enhancement of photo-piezocatalytic performance in $BaTiO_3$ via heterovalent ion doping [J]. *Advanced Functional Materials*, 2022, 32(52): 2209365.
[30] Liu L Z, Huang H W, Chen F, et al. Cooperation of oxygen vacancies and 2D ultrathin structure promoting CO_2 photoreduction performance of $Bi_4Ti_3O_{12}$[J]. *Science Bulletin*, 2020, 65(11): 934-943.
[31] Liu W, Wang P F, Ao Y H, et al. Directing charge transfer in a chemical-bonded $BaTiO_3$@ReS_2 Schottky heterojunction for piezoelectric enhanced photocatalysis[J]. *Advanced Materials*, 2022, 34(29): 2202508.
[32] Zhang D P, Li Y X, Wang P F, et al. Regulating spin polarization through cationic vacancy defects in $Bi_4Ti_3O_{12}$ for enhanced molecular oxygen activation [J]. *Angewandte Chemie International Edition*, 2023, 62(23):

e202303807.
[33] Liu S J, Zhang Z G, Dastafkan K, et al. Yttrium-doped NiMo-MoO_2 heterostructure electrocatalysts for hydrogen production from alkaline seawater[J]. *Nature Communications*, 2025, 16(1): 773.
[34] Liu Y, Chen T, Zheng J, et al. Enhanced piezo-catalytic performance of $BaTiO_3$ nanorods combining highly exposed active crystalline facets and superior deformation capability: water purification and activation mechanism [J]. *Chemical Engineering Journal*, 2024, 488: 150768.
[35] Dai B Y, Biesold G M, Zhang M, et al. Piezo-phototronic effect on photocatalysis, solar cells, photodetectors and light-emitting diodes [J]. *Chemical Society Reviews*, 2021, 50 (24): 13646-13691.
[36] Pan L, Sun S C, Chen Y, et al. Advances in piezo-phototronic effect enhanced photocatalysis and photoelectrocatalysis[J]. *Advanced Energy Materials*, 2020, 10(15): 2000214.
[37] Kumar A, Sharma P, Wang T T, et al. Recent progresses in improving the photocatalytic potential of $Bi_4Ti_3O_{12}$ as emerging material for environmental and energy applications [J]. *Journal of Industrial and Engineering Chemistry*, 2024, 138: 1-16.
[38] Tu S C, Huang H W, Zhang T R, et al. Controllable synthesis of multi-responsive ferroelectric layered perovskite-like $Bi_4Ti_3O_{12}$: photocatalysis and piezoelectric-catalysis and mechanism insight[J]. *Applied Catalysis B: Environmental*, 2017, 219: 550-562.
[39] Hou J Y, Liu H J, Zhao L. Optimization of radiation absorption model in solar photocatalytic reactors: coupling photocatalyst concentration distribution[J]. *Applied Thermal Engineering*, 2019, 160: 114090.
[40] Cai H, Hu C, Zhang X L, et al. Ultrathin $Bi_4O_5I_2$ nanosheets as an integrated piezo-photocatalyst: super visible-light piezo-photocatalysis and synergistic catalytic mechanism[J]. *Applied Surface Science*, 2023, 635: 157771.
[41] Govindan K, Kim D G, Ko S O. Role of co-existing anions in non-radical and radical processes of carbocatalyzed persulfate activation for acetaminophen degradation [J]. *Environmental Science: Water Research & Technology*, 2022, 8(12): 2940-2955.
[42] Ji B C, Li X C, Gao S, et al. Polarization-enhanced piezo-photocatalysis over hollow-sphere $Bi_4Ti_3O_{12}$: structure-property relationship and degradation mechanism[J]. *Chinese Journal of Catalysis*, 2025, 76: 133-145.

Y^{3+} 掺杂诱导钛酸铋纳米片极化增强以提升压电光催化性能用于高效水净化

杭佳和，胡春艳*，刘保江*
东华大学 绿色低碳纺织印染技术教育部重点实验室，化学与化工学院，上海 201620

摘　要：开发高效的压电光催化系统对于环境修复和废水净化具有重要意义。本研究通过结构调控的方法，将钇离子(Y^{3+})引入 Aurivillius 相钛酸铋（$Bi_4Ti_3O_{12}$，BTO）的 A 位，制备了一种新型压电光催化剂(Y-BTO)以用于协同降解盐酸四环素(tetracycline hydrochloride，TC)。结果表明，用半径较小的 Y^{3+} 取代 Bi^{3+} 引起了晶格畸变并增强了材料本征压电极化。在超声和光照同时作用下，最佳掺杂比例的 Y-BTO 催化剂表现出优异的压电光催化活性，60 min TC 去除率可达 88.8%。TC 压电光催化降解反应的表观准一级速率常数为 29.40×10^{-3} min^{-1}，分别是压电催化和光催化的 3.6 倍和 2.3 倍。这种显著增强归因于压电−光协同效应：超声振动产生的压电场有效促进了光生电子−空穴对的分离和迁移，从而大幅提高了量子效率。本研究表明，A 位离子替换是设计用于环境修复的高性能压电光催化剂的有效策略。

关键词：压电光催化；废水处理；极化增强；钇掺杂钛酸铋